

RESEARCH ARTICLE

Analysis of the Directional Characteristics of the Clumping Index (CI) Based on RAMI-V Canopy Scenes

Jinke Xie, Donghui Xie*, Kun Zhou, Guangjian Yan, and Xihan Mu

State Key Laboratory of Remote Sensing Science, Faculty of Geographical Science, Beijing Normal University, Beijing 100875, China.

*Address correspondence to: xiedonghui@bnu.edu.cn

The vegetation canopy clumping index (CI) is an important indicator for understanding radiative transport processes, radiation interception, and the photosynthesis of vegetation canopies. However, most studies consider CI only in the nadir or specific direction. In this study, we analyze the directional characteristics of the CI based on RAMI-V (radiation transfer model intercomparison) activity, which represents most typical canopies. The directional gap fraction and CI of these scenes are accurately calculated based on the LESS (large-scale remote sensing data and image simulation framework) model. According to our results, the directional characteristics of the CI are affected by many factors, such as vegetation type, season, and canopy structure. Generally, the CI of a coniferous forest varies little with zenith angle, while the CI of a broad-leaf forest demonstrates the different trend. In winter, the CI is smaller than that in summer, and the variation in the CI at the zenith angle is less. The row structure scenes exhibit different directional characteristics along and perpendicular to the row direction, and their CIs tend to increase with zenith angle. To accurately model the directional CI, we propose a modified Gompertz function model. Compared with other directional CI models, this model has the advantages of high precision and strong applicability ($R^2 = 0.975$). By studying the directional characteristics of CI, we can enhance the usability of radiative transfer modeling and the accuracy of canopy biophysical parameter retrieval for vegetation with different structures.

Introduction

Canopy structures are highly complex and variable and have a direct impact on a range of important processes, such as precipitation interception, photosynthesis, and evapotranspiration. Further, these important processes play a role in shaping global climate change [1–6]. To quantitatively describe canopy structures, several parameters have been used, including leaf area index (LAI), leaf angle distribution (LAD), and clumping index (CI). The LAI represents the amount of leaf area per unit land surface area and is defined as one half of the total green leaf area per unit horizontal ground surface [7]. Accurate field measurements of the LAI are crucial [5,8], but indirect methods of measurement are susceptible to errors arising from factors such as the LAD and clumping effects. The CI is a crucial parameter used to quantify the spatial distribution characteristics of leaves [9]. It is defined as the ratio of the effective leaf area index (LAI_e) to the true leaf area index (LAI_t), expressed as $\Omega = LAI_e/LAI_t$ [10,11]. It has been shown that the CI used in the modified Poisson model can better describe the directional gap fraction in the crown with a clustering structure [11,12]. Failure to account for the CI can lead to errors in LAI estimations of up to 70% [13–15].

At present, CI measurements mainly include remote sensing methods and field methods. Remote sensing methods estimate CI from passive optical remote sensing data through an empirical

relationship with the vegetation index (VI) or bidirectional reflectance shape indicators, e.g., the normalized difference hotspot and darkspot (NDHD) index [16–18]. Current global CI products are generated based on bidirectional reflectance distribution function (BRDF) data from moderate resolution imaging spectroradiometer (MODIS) or multiangle imaging spectrometer (MISR) with low spatial resolution (500 m or 275 m) [9,16,19–22]. One type of field measurement method estimates CI by separately estimating LAI_e and LAI_t . LAI_e is generally estimated using the canopy gap fraction method following the Beer–Lambert law [14,18,23,24], assuming that the foliage elements are randomly distributed in space [11,25]. LAI_t is obtained by destructive sampling or allometric methods, which relate the LAI with other canopy biophysical variables, e.g., diameter at breast height (DBH) for tree canopies [1].

Several optical instruments have been developed for acquiring CI with specific observation angles of vegetation canopies in the field, such as DHP (digital hemisphere photo), TRAC (tracing radiation and architecture of canopies), and LiDAR (light detection and ranging) [24,26,27]. TRAC is employed to estimate the gap fraction and gap size distribution from sunfleck measurements by walking the instrument under a canopy. The gap fraction is used to estimate the effective LAI using the Beer–Lambert law, while the gap size distribution is utilized to estimate the CI by the gap size distribution method (CC) [28]. However, TRAC can only

Citation: Xie J, Xie D, Zhou K, Yan G, Mu X. Analysis of the Directional Characteristics of the Clumping Index (CI) Based on RAMI-V Canopy Scenes. *J. Remote Sens.* 2024;4:Article 0133. <https://doi.org/10.34133/remotesensing.0133>

Submitted 31 March 2023
Accepted 5 March 2024
Published 12 April 2024

Copyright © 2024 Jinke Xie et al. Exclusive licensee Aerospace Information Research Institute, Chinese Academy of Sciences. Distributed under a Creative Commons Attribution License 4.0 (CC BY 4.0).

obtain CI at a specific zenith angle (i.e., the solar zenith angle at the time of observation) [29]. DHP and LiDAR can acquire multiple directional gap fractions and CIs. The accuracy of DHP is often affected by the light environment and exposure settings [28]. As an active remote sensing technology, LiDAR has been widely employed to measure LAI and CI, but it is greatly affected by point density and the occlusion effect [30]. Furthermore, the current methods mentioned above have some common defects. First, most existing indirect optical measurement methods are affected by factors such as solar zenith angle and observation conditions, and the measured value of CI will also change when the solar zenith angle or illumination conditions change [31]. Second, it is challenging to obtain the LAD, which is an important factor in estimating CI. In many cases, the leaf projection function G is assumed to be 0.5 [32–34]. Third, both G and CI can vary with observation angle and can interact with each other, which further complicates accurate CI measurements in the field. As a result, it can be challenging to obtain precise and reliable CI in field measurements.

Some studies have shown that the CI exhibits directional characteristics and varies with observation angle [35–37]. The directional characteristics of the CI are affected by many factors, such as vegetation type and canopy structure. For forests, the CI increases with zenith angle, ranging from 0.6 to 0.9 (Scots pines) [38,39]. Regarding three other boreal forest species, i.e., black spruce, jack pine, and aspen, the degree of clumping is dependent on the view or sun zenith angle, which is related directly to the canopy gap-size distribution; the CI increases with zenith angle in these boreal conifers, ranging from 0.4 to 1.0 in jack pine and black spruce and ranging from 0.65 to 1.0 in Aspen [5]. Concerning crops, studies have shown that the CI of maize, soybean, and sorghum increases smoothly with increasing view zenith angles while also varying with crop growth [27]. However, when using the digital hemispherical photograph (DHP) to measure the seasonal CI of regularly spaced paddy rice, some scholars have found that CI of rice canopies was basically constant (0.81) at different observation angles in early summer, which increased with zenith angle before and decreased with zenith angle after this period [38]. The variation in CI in the azimuth direction is generally considered random. Because of the complexity, most studies assume that plants are azimuthally symmetric to only consider CI variations in the zenith direction [1]. For plants or canopies with row structures, the CI also varies in the azimuth direction, in addition to the variations with the zenith angle [23,40]. The directional characteristics of CI have been expressed using various models, such as the sigmoid model [24], sinusoidal model [39], or simply a linear model [27]. All these models derive the directional variations in CI as a function of the nadir CI or the CI of a specific observation angle.

With the development of radiative transfer (RT) modeling, simulation can be used to study complex vegetation structure parameters. Three-dimensional (3D) RT modeling has become a key tool in studying the radiometric characteristics of the Earth's surface [41,42]. Over the past few decades, a number of 3D RT models have been designed to simulate the radiometric properties of landscapes [43], including DART (discrete anisotropic radiative transfer) [44] and LESS (large-scale remote sensing data and image simulation framework) [44]. These models work with relatively realistic landscapes [45]. In particular, LESS is capable of parameterizing realistic 3D scenes with high accuracy, and it is easy for LESS to simulate remote

sensing signals, such as multispectral images and bidirectional reflectance factors (BRFs) [45].

The construction of a high-precision, parameterized scene is a crucial component of a 3D RT physical model. The radiation transfer model intercomparison (RAMI) initiative proposes a mechanism to benchmark models designed to simulate radiation transfer at or near the Earth's terrestrial surface. The fifth RAMI phase (RAMI-V) provided both abstract and actual scenes, representing various canopies, including homogeneous and heterogeneous vegetation structures.

The objective of this study is to use LESS to compute the LAD, directional gap fraction, and CI of complex 3D vegetation scenes at different observation angles. Additionally, we aim to summarize the directional characteristics of the CI for canopies with typical canopy structures and propose a universal directional model for the CI. This study has the potential to enhance our understanding of the clumping effects of different canopy structures while enriching the RAMI dataset.

Materials and Methods

3D scenes from RAMI-V

As an open, self-organizing activity of the canopy RT modeling community, since 1999, the RAMI exercise has been focused on the evaluation of models simulating BRFs and radiative fluxes for 1D and 3D vegetation canopies [46,47]. To date, five phases of RAMI have been conducted. RAMI-V proposed 38 canopy scenarios, which are subdivided into abstract and actual canopies. An overview of the canopy scenes is given in Table 1. Abstract canopies contain both homogeneous (HOM) and heterogeneous (HET) leaf canopies that are both exclusively composed of disc-shaped finite-sized scatterers. Actual canopies are reconstructed from detailed inventories of the structural properties of existing plantations and forest stands. These diverse structural scenes have explicit structures, including leaves, branches, and stems.

RAMI delivers the data and information of the scenes in human readable format (generic) to allow different standards/hance different models to participate some basic geometries. Although the format provided by RAMI is more general and assumes no assumptions, unfortunately LESS does not currently accept RAMI's human readable geometry. Zhou *et al.* [48] transferred the structure and radiometric information into Wavefront (OBJ) open file format by introducing some assumption and approximation of the original scene while maintaining the same simulation accuracy. They replaced the regular octagon and hexagonal prismoid with the disc and cylinder structures, and split the ellipsoid into two hexagonal pyramids [48]. The surface area of all the simplified geometries is the same as that of the original geometries. The structure of an entire scene is reconstructed through 3D transformation operations, including rotation, translation, and scaling of the simplified basic geometries to obtain each component of a single tree (such as branches and leaves). A twig or leaf is taken as a template to generate trees with leaf elements, and various individual trees are copied into the planting coordinate system by translation and rotation. These reconstructed scenes are applied in the LESS RT model to probe the ability of its RT solvers to simulate all sorts of remote sensing observations and radiative budgets, including the BRF, albedo, fraction of photosynthetically active radiation absorbed by vegetation, and DHP. The result is well validated by the RAMI Online Model Checker (ROMC) reference data and Rayspread model for the abstract and actual scenes. This scheme not only

efficiently produces negligible simulation errors with less computational resource consumption but also ensures the consistency of the projected area. Information details regarding the transformation of 3D scenes can be found in [48].

This paper uses the implementation of the scenes provided by Zhou *et al.* to study the directional characteristics of CI at quadrat scale based on RAMI scenes (<https://rami-benchmark.jrc.ec.europa.eu>), the details of which can be found in Table 1.

Parameter calculation based on the LESS model

Due to the strong heterogeneity of HET50 (savanna), it does not meet the assumptions on Beer's law, so HET50 is not considered in this study; for the other 37 scenes, we obtained the LAD and subsequently calculated the leaf projection function (G). Next, using the LESS model, we calculated the gap fraction for 37 scenes in RAMI at various observation angles. Finally, the directional CI was calculated according to G and gap fraction.

LESS model

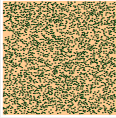
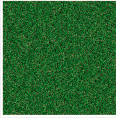
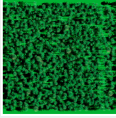
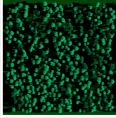
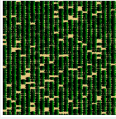
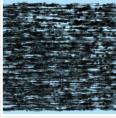
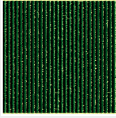
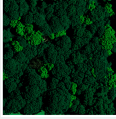
LESS is a large-scale RT model based on a ray tracing algorithm. It can simulate many remote sensing signals (i.e., reflectance image, fisheye photos, BRDF, albedo, and fraction of photosynthetically active radiation) and land surface parameters (i.e., LAI, LAD, and directional gap fraction) based on 3D structural canopy scenes. In this study, LESS is used to accurately calculate the directional gap fraction, LAI, and LAD and then acquire directional CIs.

Directional gap fraction

The directional gap probability or gap fraction is a basic parameter in optical remote sensing modeling. The gap fraction can be obtained by reclassification of simulated images; however, the heterogeneity of canopies and resolution of images can impact the accuracy of extracted gap fraction due to the mixed pixel issue [49].

To avoid the issues that extraction of gap fraction is affected by the image resolution, the sampling method is used in the

Table 1. Overview of the RAMI canopy scenes shown in the paper. LAI-calculated is the true LAI calculated by LESS, and Orthophoto refers to the Orthophoto rendered by LESS.

Type	RAMI-ID	LAI-calculated	Orthophoto	Description
Abstract	HET10	0.9805		Randomly distributed spherical crown
	HOM23	1		Homogeneous canopies composed of a large number of nonoverlapping disc-shaped objects representing the foliage elements
Actual	HET07	2.2839		<i>Pinus sylvestris</i> forest (124 years old)
	HET09	3.4552		<i>Betula pendula</i> forest (49 years old) (summer)
	HET14	2.6913		Citrus orchard located in Wellington, South Africa (9 years old)
	HET15	0.0336		<i>B. pendula</i> forest (49 years old) (winter)
	HET16SRF	3.2086		A short rotation forest of poplar clones
	HET51	7.3396		Wytham Woods 3D model, which represents a one-hectare deciduous forest in Wytham, UK

LESS model to calculate the gap fraction of canopy scenes accurately. Figure 1 shows the principle for LESS to calculate the gap fraction. Once the illumination and view angles are determined, the interaction between direct solar light and canopy primitives can be partitioned into four distinct components through a ray tracing algorithm when only direct solar light is considered, i.e., sunlit foliage, shaded foliage, sunlit background, and shaded background, which are the main parameters in geometric optical (GO) models [50]. In the LESS model, the simple probability sampling method is applied to statistically analyze the area ratios of four components (sunlit foliage $P_{\text{foliage}}^{\text{sunlit}}$, sunlit background $P_{\text{background}}^{\text{sunlit}}$, shaded foliage $P_{\text{foliage}}^{\text{shaded}}$, and shaded background $P_{\text{background}}^{\text{shaded}}$) in the canopy scene. The rays are randomly cast from each pixel to the scenes, and the first intersections between the rays and objects (foliage or background) in the scene are projected to the solar incident direction. Subsequently, they are checked to see if the intersections are lit or shaded and then recorded. Next, we can obtain accurate ratios of the four components in each pixel. According to the simulated four-component data, the directional gap probability $P(\theta, \varphi)$ can be calculated as follows:

$$P(\theta, \varphi) = \frac{\sum_{i=1}^n \left(P_{\text{background}}^{\text{sunlit}}(\theta_i, \varphi_i, \theta, \varphi) + P_{\text{background}}^{\text{shaded}}(\theta_i, \varphi_i, \theta, \varphi) \right)}{n} \quad (1)$$

where n is the number of pixels, θ is the view zenith angle, φ is the view azimuth angle, θ_i and φ_i are the illumination and azimuth angles, respectively. The illumination (θ_i and φ_i) in

Eq. 1 only affects the proportion of the sunlit background and the shaded background, while the sum of the two, that is, the gap fraction, will not change with the illumination change, so although LESS calculates the gap fraction based on four components, in fact, it is only affected by the observation angle.

The directional gap fraction can be obtained by adjusting the observation angle in the LESS model. We divided the observation angles into 325 directions with an interval of 10° for both zenith and azimuth angles in the upper hemispheric space to obtain the complete dataset of the directional gap fractions.

LAD and directional CI

The LAD is described by the probability density function $g(\theta_l, \varphi_l)$, which should satisfy the normalization expressed in Eq. 2 as follows [32]:

$$\frac{1}{2\pi} \int_0^{\frac{\pi}{2}} d\varphi_l \int_0^{\frac{\pi}{2}} g(\theta_l, \varphi_l) d\theta_l = 1 \quad (2)$$

where θ_l and φ_l represent the zenith and azimuth angles of the leaf, respectively.

Based on the OBJ file and related attribute information provided by RAMI (the number of different tree species within the canopy), each leaf normal vector and leaf area can be calculated, and then the LAD function $g(\theta_l, \varphi_l)$ is obtained by a statistical method.

The leaf projection function (G) is defined as the projection coefficient of the unit leaf area on a plane perpendicular to the observation direction and is expressed as Eq. 3.

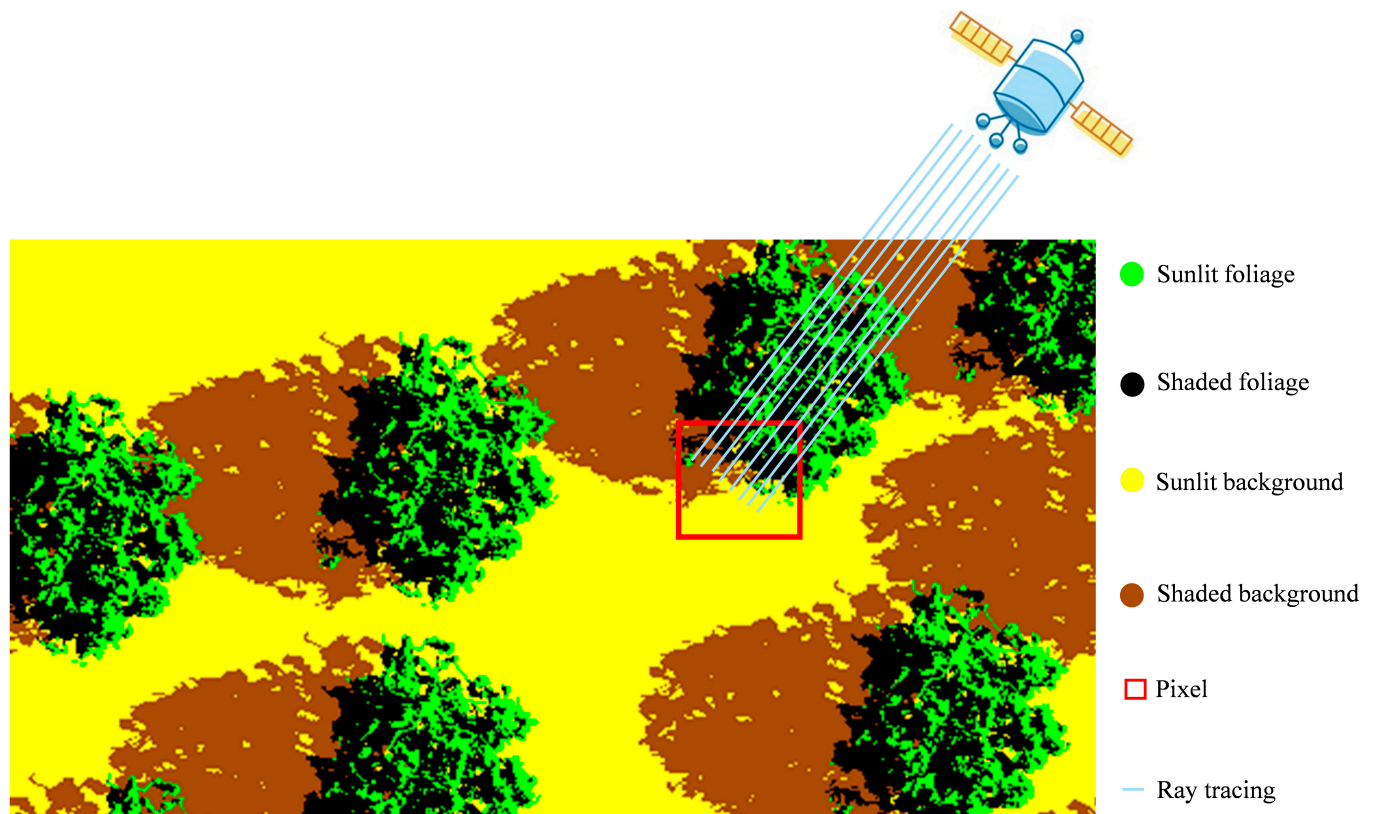


Fig. 1. Once the illumination and view angles are determined, LESS calculates the proportions of the four components within each pixel (red rectangle) using ray tracing and subsequently generates the four-component images. In the figure, different colors signify different component, and gap fractions are calculated based on the ratios of the four-component images within a pixel.

$$G(\theta, \varphi) = \frac{1}{2\pi} \int_0^{2\pi} d\varphi_1 \int_0^{\frac{\pi}{2}} g(\theta_1, \varphi_1) |r_1 \cdot r| d\theta_1 \quad (3)$$

where θ and φ are the zenith and azimuth angles of the observation direction, respectively. $|r_1 \cdot r|$ represents the dot product of the blade normal vector r_1 and the observation direction r and is expressed as Eq. 4.

$$|r_1 \cdot r| = \cos(\theta)\cos(\theta_1) + \sin(\theta)\sin(\theta_1)\cos(\varphi_1 - \varphi) \quad (4)$$

Since most canopy blades are approximately evenly distributed in the azimuth direction, only the zenith angle of the blade is usually measured to describe the angle distribution of the blade [51]. The azimuthal change in the leaf projection function is considered in this study.

CI is generally derived with the Beer–Lambert law [11].

$$P(\theta, \varphi) = e^{-\frac{G(\theta, \varphi)\Omega(\theta, \varphi)LAI_t}{\cos(\theta, \varphi)}} \quad (5)$$

where LAI_t is the true LAI accurately calculated based on the OB files by LESS. Considering the variation in CI in both the zenith and azimuth directions, the directional CI is calculated as Eq. 6.

$$\Omega(\theta, \varphi) = \frac{-\ln P(\theta, \varphi)\cos(\theta)}{G(\theta, \varphi)LAI_t} \quad (6)$$

Directional CI model

Generally, it is difficult for existing measurement methods to calculate directional CIs at all observation angles. To address this, some studies have proposed models to fit CIs under different zenith angles, as shown in Table 2. Among them, the Montes and Kucharik models do not require empirical parameter estimation. The Montes model only uses the CI in the nadir direction to estimate directional CIs [39], while the Kucharik model determines empirical parameters based on different tree species as prior knowledge and then uses the CI of a large zenith angle as an input parameter to estimate directional CIs [5]. The other four models require multiple CIs at different zenith angles to fit empirical parameters for modeling and estimating directional CIs. However, current models are derived from indirect measurement methods and may have low stability due to factors such as vegetation species and canopy structure. Therefore, in this study, we proposed two new models based on the CI derived from RAMI-V scene analysis (note: RAMI does not deliver explicit CI values), one of which is a modification of the model

Table 2. The existing directional CI models. Some scholars have proposed directional CI models based on various vegetation types. These models often rely on empirical relationships between directional CI and CI at specific observation angles (such as nadir direction, etc.).

Model	References
$\Omega(\theta) = \Omega(0) + a\theta$	Fang et al. [27,38]
$\Omega(\theta) = \Omega(0) + \frac{\Omega_{\max} - \Omega_{\min}}{1 + e^{-a(\theta-b)}}$	Duthoit et al. [24]
$\Omega(\theta) = \Omega(0)\cos^2(\theta) + \sin^2(\theta)$	Montes et al. [39]
$\Omega(\theta) = \Omega(0) + a(1 - \cos(\theta))$	Pinty et al. [54]
$\Omega(\theta) = \frac{\Omega_{\max}}{1 + be^{-k\theta}}$	Kucharik et al. [5]

proposed by Montes et al. in 2007, and the other is a new model based on the Gompertz curve.

While the model proposed by Montes et al. [39] has the advantages of being simple and represent clumping variation against the zenith angle with only one parameter, it has a limitation in that it assumes that the CI approaches 1 when the zenith angle approaches 90°, which is not accurate for many canopies. To address this issue, we added a new parameter Ω_{\max} to the model. By incorporating this additional knowledge, the Montes model is modified to achieve better accuracy and retain the expected trend of CI changes as the zenith angle increases. The modified Montes model is shown in Eq. 7.

$$\Omega(\theta) = \Omega(0)\cos^2(\theta) + \Omega_{\max}\sin^2(\theta) \quad (7)$$

where $\Omega(0)$ is the CI in the nadir direction and Ω_{\max} represents the CI when the zenith angle approaches 90°.

The Gompertz model is one of the most frequently used sigmoid models, which is often fitted to the growth of many living things [52]. One valuable and commonly found parameterization is shown in Eq. 8.

$$f(t) = d + ae^{-e^{b-ct}} \quad (8)$$

where $f(t)$ is the expected value (mass or length) as a function of time t . There are four parameters to control the model. d represents the lower asymptote of the curve, a represents the upper asymptote, b represents time at inflection, and c represents a growth-rate coefficient (which affects the slope).

To apply the Gompertz curve to the fitting of CI, we change the parameterized form to Eq. 9.

$$\Omega(\theta) = \Omega(0) + (\Omega_{\max} - \Omega_{\min})e^{-e^{b-c\theta}} \quad (9)$$

where $\Omega(0)$ is the CI in the nadir direction and Ω_{\max} is replaced by the CI when the zenith angle approaches 90°. Ω_{\min} is considered to be equal to $\Omega(0)$.

Results and Discussion

In this section, we calculated the LAI, leaf projection function G , directional gap fraction, and directional CI based on 3D reconstructed scenes. Out of the 37 scenes in RAMI, we selected 8 typical scenes to show and analyze the results, including HET10 (randomly distributed spherical crown canopy) and HOM23 (homogeneous canopy) among abstract canopies and HET07, HET09, HET14, HET15, HET16SRF, and HET51 among actual scenes. These eight scenes basically cover typical canopy scenes with a variety of structures and tree species, including the coniferous forest (HET07), broad-leaved forest (HET14, HET16SRF, HET51), and mixed forest (HET09, HET15) of different seasons and row structure scenes.

Leaf projection function

It is evident from Fig. 2, in scenes other than HET51, the leaf area projection function remains relatively constant at various azimuths, we calculated the standard deviation of G in the azimuthal direction for different viewing zenith angles, the standard deviation of G in scenes other than HET51 are below 0.011, while the standard deviation of G in the azimuthal direction in HET51 increases with the view zenith angle from 0 to 0.065. Hence, for HET51, the impact of G on the azimuth angle is not negligible, and the effect of G on the calculation of the directional CI can be effectively mitigated by accurately computing the true value of G .

The variations in G with zenith angles exhibit different characteristics, as shown in Fig. 3. It is evident that there are various

types of LADs present in the RAMI scenes and that the differences in LADs between scenes are relatively large. To better analyze these differences, we divided the eight scenes into three groups based on the characteristics of their LADs and leaf projection functions. First, the LAD of HET10 (a randomly distributed spherical canopy scene) and HET14 (the citrus orchard in summer) showed a standard spherical distribution, with G almost equal to 0.5 (Fig. 3A). Second, the LAD of HET07 (*Pinus sylvestris* forest in summer) and HET15 (a mixed forest in winter whose LAD mainly depended on spruce) demonstrated characteristics of both erectophile and spherical distributions, and G gradually increased from 0.48 to 0.51 with the zenith angle. Third, the homogeneous canopy HOM23 showed a standard planophile distribution, and G decreased from 0.84 to 0.28 with the zenith angle. HET09 (a birch forest in summer), HET16SRF (a rotation forest in summer), and HET51 (a deciduous forest in summer) showed different degrees of a planophile distribution. Notably, the growth state of vegetation and season can also affect the LAD in HET09 and HET15, which are the same forest in different seasons. They exhibit completely different LADs (Fig. 3B and C).

In coniferous forests, the LAD generally exhibits an erectophile distribution, while in broadleaved forests, the LAD is more variable, demonstrating features from spherical, planophile, or plagiophile distributions, for example. To further explore the LAD of different tree species, we calculated G of different tree species based on HET09 (a mixed forest), and the results are shown in Fig. 3D. HET09 consists of seven species of trees, including maple (ACPL), white birch (BEPE), alder (ALGL), lime (TICO), poplar (PORT), ash (FREX), and spruce (PIAB), all of which are broadleaved trees except spruce (PIAB). The LAD distribution of spruce (PIAB) exhibited the characteristics of both the spherical distribution and the erectophile distribution.

Maple (ACPL) showed the standard erectophile distribution, while G of other broad-leaved trees showed a similar trend, and G decreased with the zenith angle. For coniferous forests, the G values are all approximately 0.5 under different projection angles, and the directional characteristics are not obvious. However, for broadleaved forests, the G values are greatly affected by projection angles, and the difference in G between the minimum (0°) and maximum (90°) zenith angles can reach 0.8. The G values of different broadleaved trees also vary greatly. For example, maple (ACPL), as a broadleaved tree, exhibited a typical LAD with an erectophile distribution, and its G increased with increasing zenith angle. In contrast, the LAD of other broadleaved trees mostly showed signs of both planophile and spherical distributions, and G decreased with increasing zenith angle.

Directional gap fraction

The directional gap fractions are calculated based on the four-component image simulated by the LESS model. The directional gap fractions from eight scenes are shown in Fig. 4.

In general, the directional gap fractions of different scenes are closely related to the fraction of vegetation cover (FVC) and LAI [53]. According to Table 3, we can infer that the average gap fraction was negatively correlated with the LAI. Scenes with higher LAIs have a higher FVCs and thus smaller gap fractions. For example, the gap fraction of HET10 with a small LAI was as high as 0.8 in the nadir direction (Fig. 4C). The LAI of HET15 was small in winter but had a large plant area index (PAI), so the gap fraction was higher than that of the other scenes with low LAIs (Fig. 4E). The LAI of HET51 was as high as 7.34, and its gap fraction was less than 0.1 under different observation directions (Fig. 4G).

Considering the directional characteristics of the gap fraction, all non-row structure scenes show a trend of gap fraction

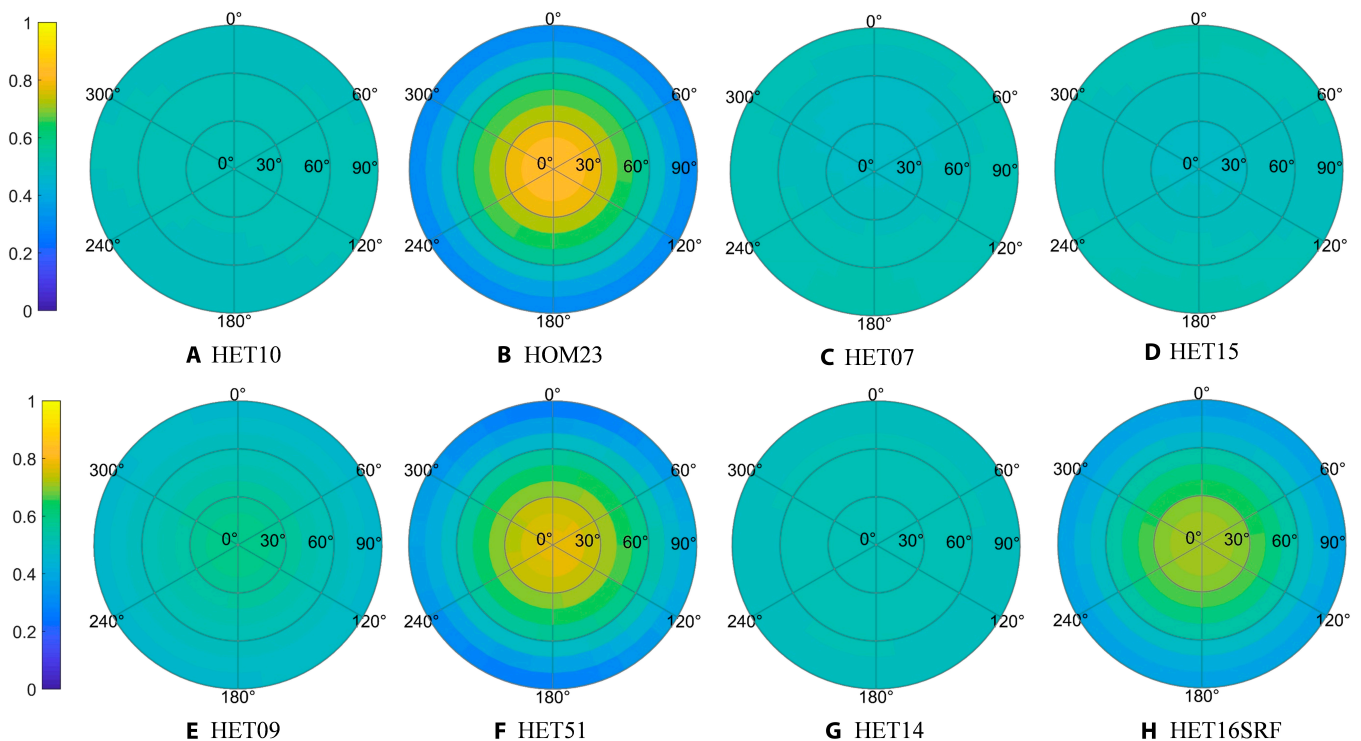


Fig. 2. (A to H) The leaf projection function (G) distributions from eight scenes. HOM23 and HET10 (abstract canopies), HET07 and HET15 (pines), HET09 and HET51 (broadleaf forests), and HET14 and HET16SRF (crops). The leaf projection function (G) is depicted in polar coordinates. The color transitions from blue to yellow as G consistently increases.

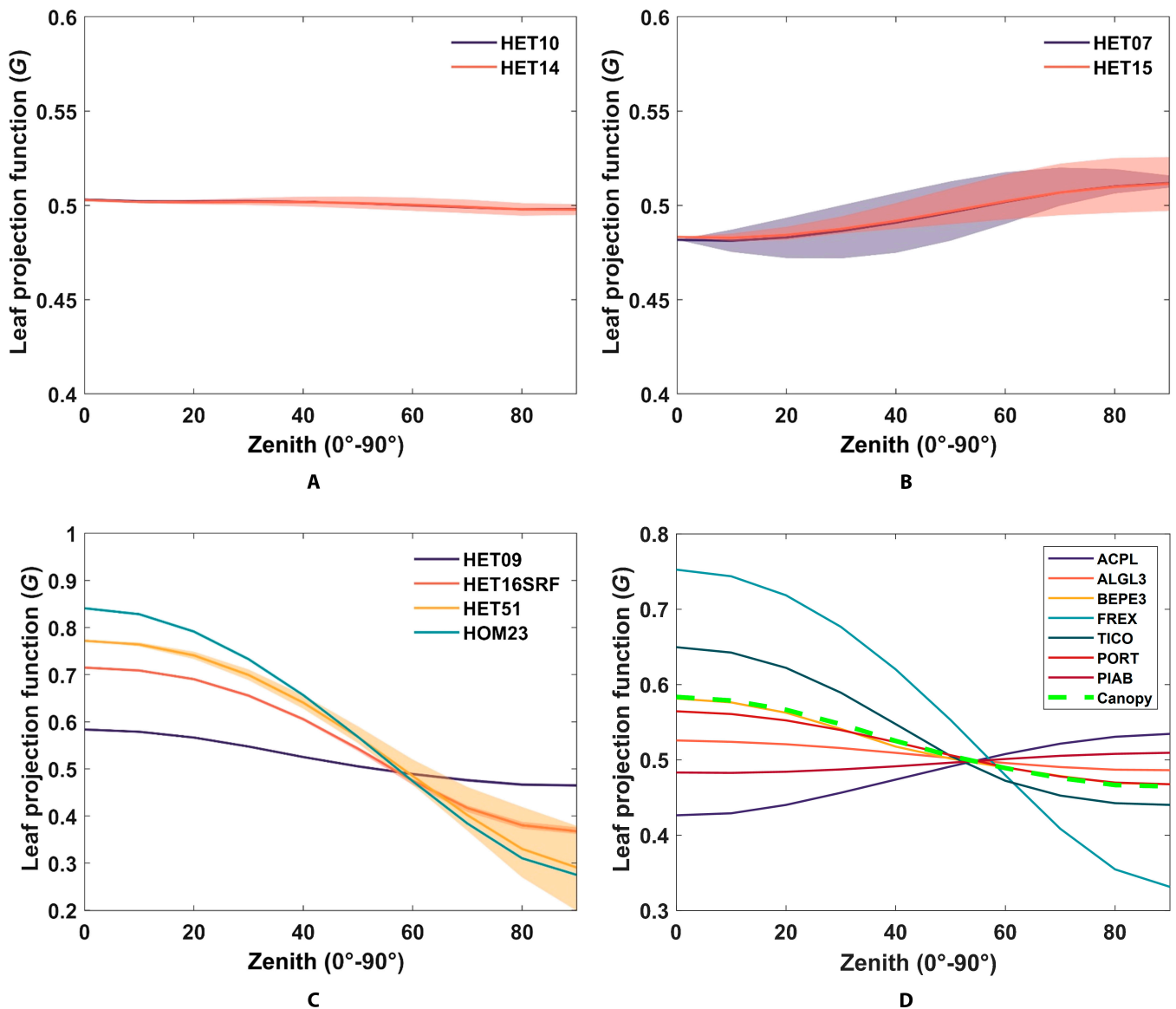


Fig. 3. The variation in the leaf projection function (G) on the zenith angle. (A to C) G of whole canopies in different scenes. The solid line represents the average value of G at different azimuths, and the shadows are the maximum and minimum values at the azimuths. (D) G of different tree species in HET09. The green dashed line represents the average value of G for the entire HET09.

decreasing with increasing zenith angle, and the amplitude of this variation depends on canopy LAI. The larger the LAI is, the smaller the variation trend of the gap fraction on the zenith angle. The variability of the gap fraction against the zenith angle for the row structure crops (HET14, HET16SRF) is completely different along the row direction and perpendicular to the row direction (Fig. 4D and F). Along the row direction, the gap fraction does not change with the zenith angle, while for the direction perpendicular to the row direction, the gap fraction decreases with the zenith angle.

Clumping index

The directional CIs from the eight scenes are shown in Fig. 5, and several characteristics of CI can be found from these canopy scenes. Being an indicator of the randomness of spatial leaf distribution, the CI of the homogeneous canopy (HOM23) is expectedly close to and does not vary with the observation direction (Fig. 5H). This indicates that there is no clumping effect in HOM23, so it is not analyzed in the remaining part of the paper.

Second, the CIs of the other seven heterogeneous scenes from different observation directions are all less than 1, which means that there are different degrees of clumping effects. Third, in the azimuth angle, we observe that, in all scenes, the azimuth angle shows a periodic pattern with an increase from 0° to 45° followed by a decrease from 45° to 90° . This pattern arises from the canopy layers used in this paper, with a distance of 0 to 3 m between the canopy layer and the scene's edge. When the observation zenith angle is large, LESS employs a method of scene replication to prevent observations from exceeding the scene boundaries. However, due to the presence of the scene's edge spacing mentioned earlier, the gap fraction is still influenced by the observation azimuth angle. This effect is more pronounced with larger scene margins, such as HET09, and less pronounced with very dense tree canopies, such as HET51. Without considering the periodic errors introduced into the scene, the CI of non-row structure has irregular variations in the azimuth such as HET51, while for the row structure scenes (HET14, HET16SRF), the CI difference was substantial in the azimuth, the CI decreased significantly along

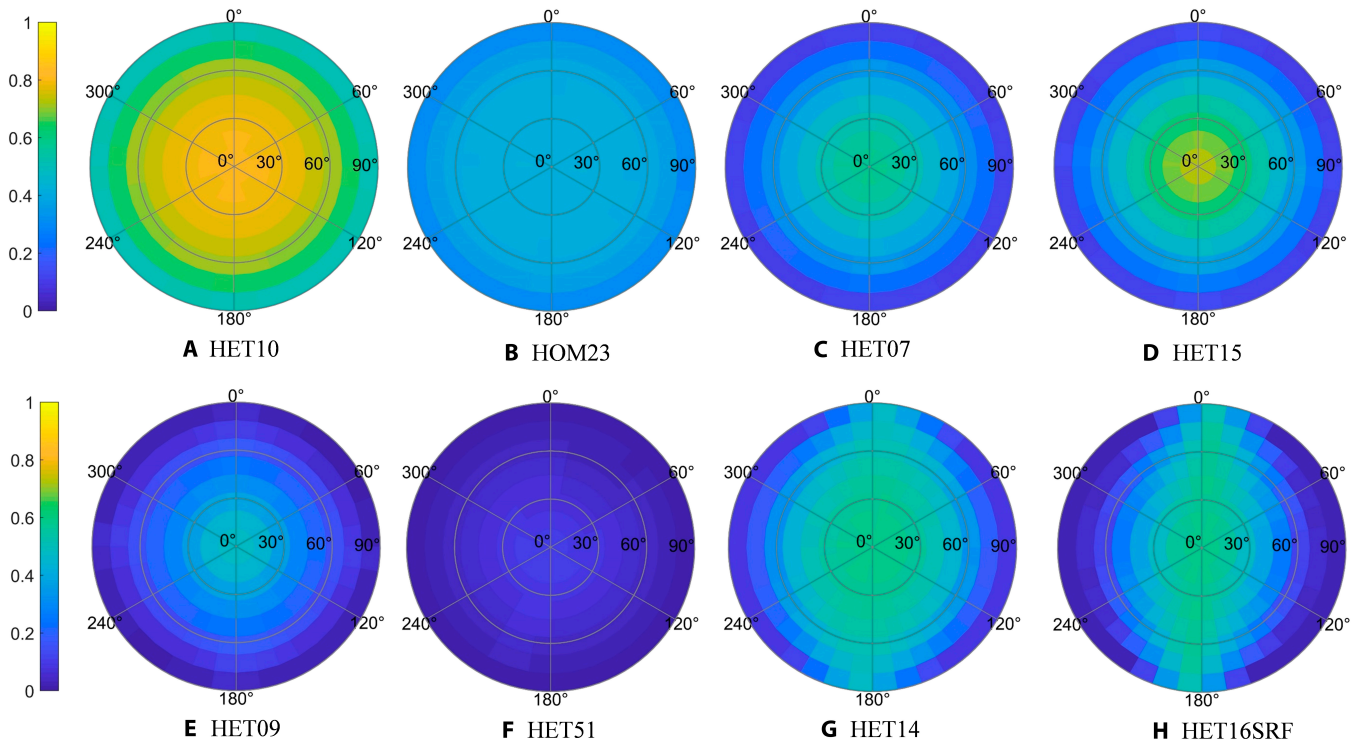


Fig. 4. (A to H) The directional gap fractions from eight scenes, including HET10 and HOM23 (abstract canopies), HET07 and HET15 (pines), HET09 and HET51 (broadleaf forests), and HET14 and HET16SRF (crops). The directional gap fractions are depicted in polar coordinates. The color transitions from blue to yellow as gap fractions consistently increase.

Table 3. The true LAI and average gap fractions from eight scenes. Here, LAI excludes the impact of woody components, while gap fraction calculations include the influence of PAI. As a result, HET15 demonstrates a relatively low gap fraction even at extremely low LAI due to the effect of PAI.

	HET10	HOM23	HET07	HET15	HET09	HET51	HET14	HET16SRF
LAI	0.9805	1.0000	2.2839	0.0336	3.4552	7.3396	2.6913	3.2086
Gap fraction	0.669	0.366	0.355	0.418	0.249	0.0517	0.407	0.349

the row direction (0° to 180°), and the clumping effect was significant, while the CI in the direction perpendicular to the row direction increased significantly.

Once averaged over the azimuth angle, one can appreciate the variability over zenith angle as shown in Fig. 6. Figure 6A shows that the CI of HET10 remained almost unchanged and was equal to 0.45 under different observation angles. HET10 was composed of a randomly distributed spherical crown canopy. Moreover, the LAD of each crown is spherical, so $-\ln P(\theta, \varphi) \cos \theta$ and G hardly change with changing observation angle. Similar to HET10, there are many other scenes composed of randomly distributed spherical canopies (HET12, HET16, HET26, etc.), which either have different leaf area densities or are composed of different sizes of spherical canopies, but all meet the homogeneous distribution characteristics of scatters (leaves); therefore, CI is approximately equal to 0.5 under different observation angles. Therefore, the results are not plotted here.

Figure 6B shows the results of scenes HET14 and HET16SRF with row structures. Clearly, the mean value of the CI of scenes with row structures also follows the general law of increasing with zenith angle, but the variation trend of CI with zenith angle is different at azimuth angles. Figure 5G and H shows that along

the row direction (0° to 180°), CI decreases with increasing zenith angle, and when the observation is perpendicular to the row direction (90° to 270°), CI increases with increasing zenith angle.

The CI of the other non-row structural heterogeneous scenes showed increasing trends with the zenith angle (Fig. 6C and D). The CIs of HET07 composed of mainly coniferous stand changed little with the zenith angle. The difference between the maximum and minimum values was approximately 0.3 (Fig. 6C). The CI of HET51 (Fig. 6C) and HET09 (Fig. 6D) composed of broad-leaf stand changed relatively greatly. The CI of HET09 varied between 0.3 and 1, while the CI of HET51 varied between 0.4 and 0.8. HET09 and HET15 are the same forest in summer and winter. As shown in Fig. 6D, the CI of the same forest in winter is significantly lower than that in summer, and the rangeability is also significantly reduced. Due to the winter leaf-shedding of broad-leaved trees, the contribution of wood components to the gap fraction increases significantly. Consequently, the CI is also influenced by the interaction between the wood components of deciduous trees and the leaf elements of coniferous forests. When considering the inclusion of wood components, the study of the CI becomes more intricate; hence, we will refrain from delving further into this matter.

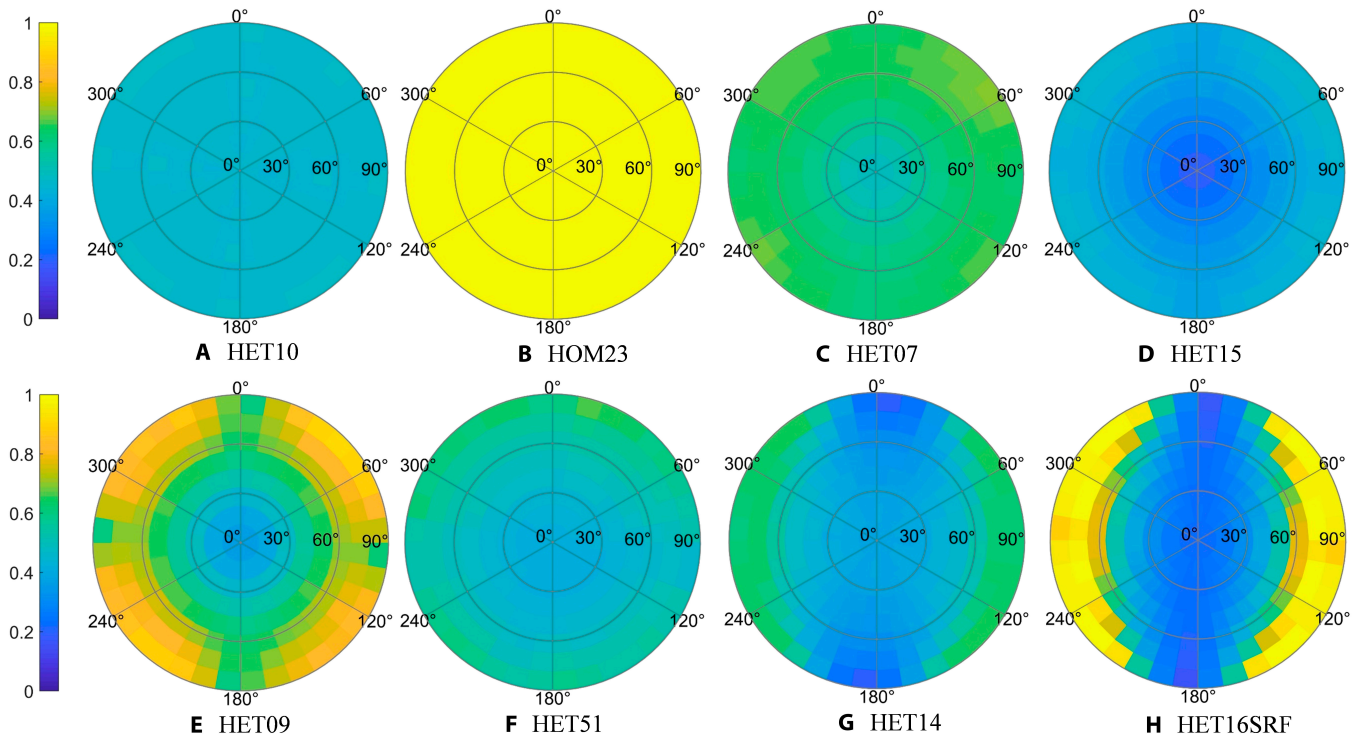


Fig. 5. (A to H) The directional Cls from eight scenes, including HET10 and HOM23 (abstract canopies), HET07 and HET15 (pines), HET09 and HET51 (broadleaf forests), and HET14 and HET16SRF (crops). The directional Cls are depicted in polar coordinates. The color transitions from blue to yellow as Cl consistently increases.

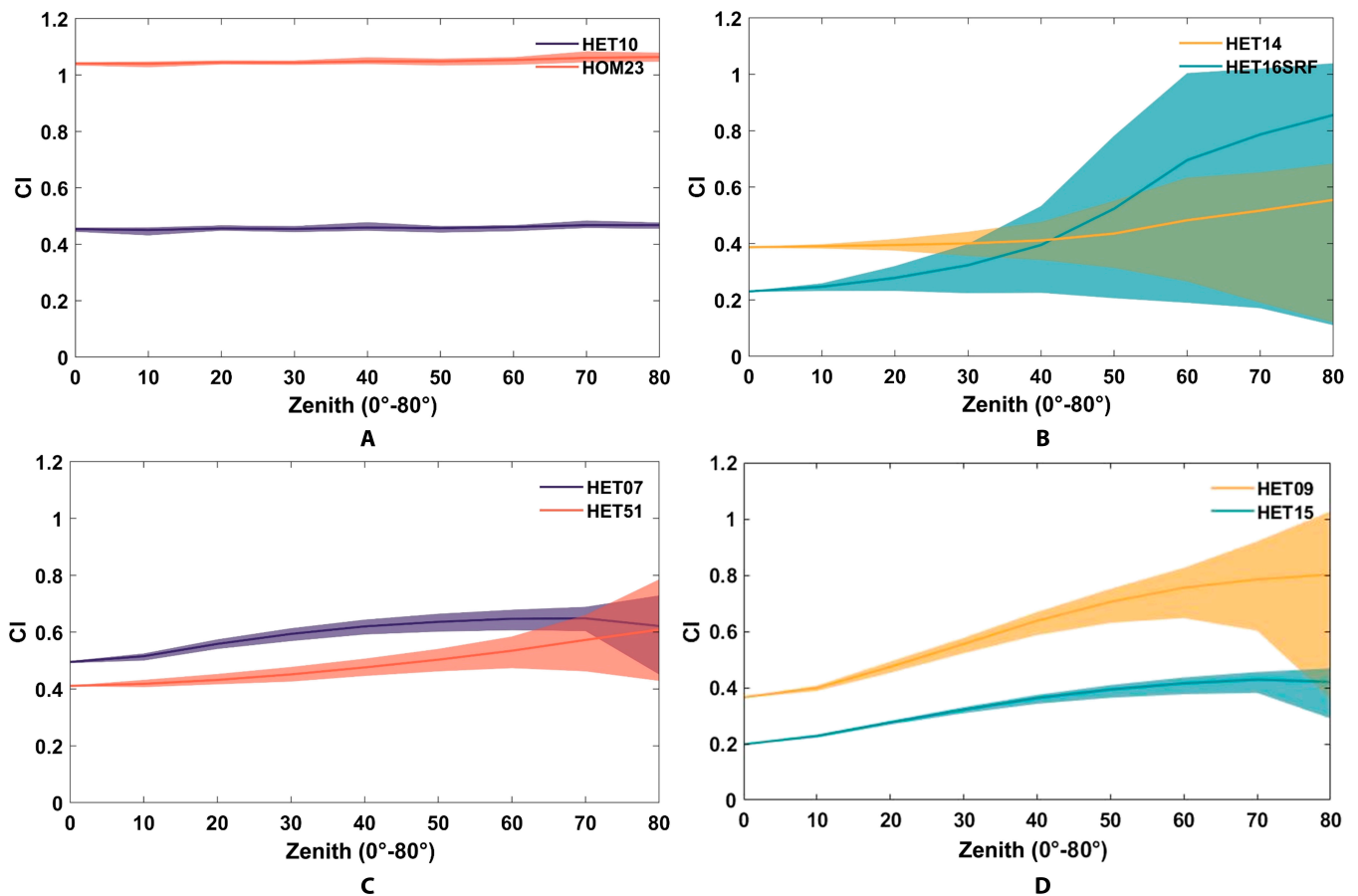


Fig. 6. (A to D) The variation in directional Cl with zenith. The solid line represents the mean value of Cl under the zenith angle, and the upper and lower edges of the strip section represent the maximum and minimum values of Cl, respectively.

Downloaded from <https://spj.science.org> on April 29, 2024

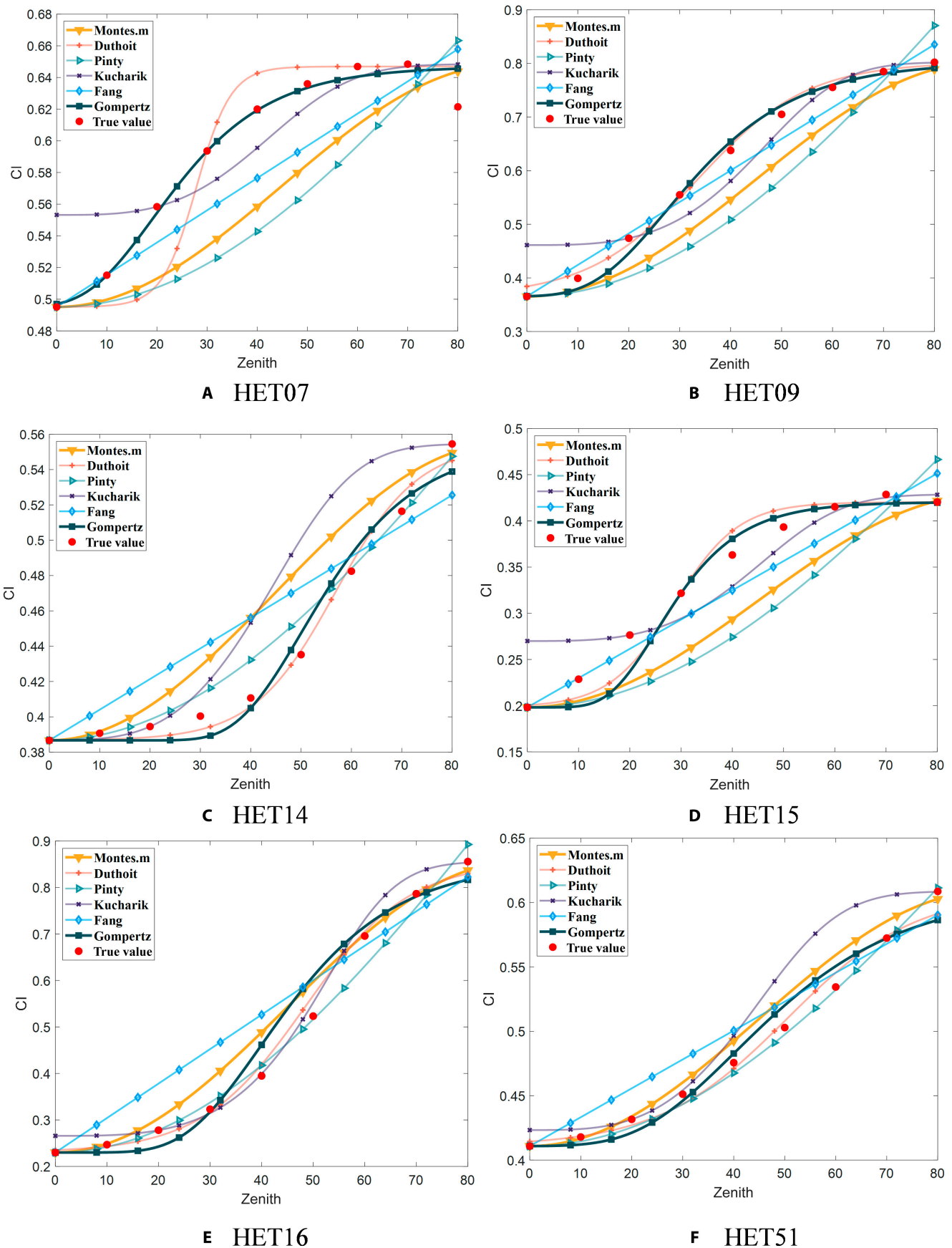


Fig. 7. (A to F) Fitting of directional characteristics of the CI using different models. Six actual scenes were chosen to illustrate the results of the directional CI model. The red dots represent the true CI calculated using LESS, while the predictions of the six models are depicted with various line types and colors.

Fitting with the CI model

Here, the directional CIs of the six scenes except for HET10 and HOM23 (for which we found rather obvious behavior) are fitted with the six directional CI models listed in Table 2, including those existing models and the two models proposed in this study. Then, we compare and analyze the fitting accuracy of different models.

For all the directional CI models, $\Omega(0)$ is the CI in the nadir direction, and Ω_{max} is the CI at a zenith angle of 80° . For the Kucharik model [5], the empirical parameters are $b = 0.4379$, $k = 2.2$, and $p = 3.34$. To solve the empirical parameters, the other four models were fitted with four CIs at zenith angles of 0° , 30° , 60° , and 80° .

In Tables 4 and 5, the Gompertz model with highest average R^2 values (0.975) and low average RMSE (0.0176) shows the better fitting results than most other models. Its fitting curves are highly consistent with the directional characteristics of CI in zenith angles of almost all scenes. Duthoit's model exhibits good performance with high fitting accuracy in the five broad-leaved and mixed stands, except for HET07 (coniferous stand). This indicates that Duthoit's model is more suitable for broad-leaved forests than coniferous forests. Pinty's model shows good fitting results in scenes with the row structure scenes (HET14), indicating its suitability for row structure plants but even HET51 presenting the best root mean square error (RMSE) performance. On the other hand, the Fang model shows good fitting results for HET09 and HET15. Although the fitting accuracies of Kucharik's model and the modified Montes model are low, their formulas are simple and have fewer empirical parameters than the other CI models, which enables them to be applied when the observation angle is insufficient. In addition, for the HET51 scene, the fitting results of all CI models

show lower uncertainty, so we believe that the directional characteristics of the CI from the forest with a high LAI ($LAI \approx 7$) can be fitted by any model.

Conclusion

We built a complete set of leaf projection functions, directional gap fractions, and CI data from 37 scenes with various canopy structures provided by RAMI using the LESS model. The data are available at <http://lessrt.org>. The directional characteristics of CI were analyzed carefully. Two directional CI models are proposed, including the Gompertz curve model and the modified Montes model.

First, the leaf projection function of coniferous forests (HET07, HET08, HET15) usually exhibits characteristics of both erectophile and spherical distributions, while the leaf projection function of broadleaved forests can differ significantly between different tree species. At the same time, with the change in seasons, the leaf projection function of the forest will change due to the change in leaf element composition caused by defoliation. Second, the gap fraction of non-row structure canopies does not vary with the azimuth angle, but it decreases with increasing zenith angle. In contrast, for row structured canopies, the gap fraction along the row direction remains almost constant for varying zenith angles. However, the gap fraction perpendicular to the row direction decreases as the zenith angle increases. Third, although the CI varies among different canopies, all of them show a general law of increasing with increasing zenith angle. Notably, the directional characteristics of the CI in row structure scenes (HET14, HET16SRF) are complex; along the row direction, the CI slowly decreases with increasing zenith angle, while in the

Table 4. R^2 of directional CI models. Quantitative representation of the results in Fig. 7, highlighting the maximum R^2 for the predictions of six models across six scenes in boldface and the second highest in italics.

	HET07	HET09	HET14	HET15	HET16SRF	HET51
Montes.M	0.44	0.88	0.78	0.68	0.96	0.96
Duthoit	<i>0.9</i>	0.99	0.98	0.96	0.99	0.99
Pinty	0.21	0.8	0.96	0.6	0.98	0.99
Kucharik	0.49	0.91	0.75	0.75	0.99	0.87
Fang	0.69	0.97	0.62	0.91	0.83	0.9
Gompertz	0.98	0.99	0.98	0.96	0.97	<i>0.97</i>

Table 5. RMSE of directional CI models. Quantitative representation of the results in Fig. 7, highlighting the minimum RMSE for the predictions of six models across six scenes in boldface and the second lowest in italics.

	HET07	HET09	HET14	HET15	HET16SRF	HET51
Montes.M	0.040	0.053	0.027	0.046	0.046	0.014
Duthoit	<i>0.021</i>	0.012	0.009	0.017	0.02	<i>0.008</i>
Pinty	0.051	0.078	0.011	0.058	0.028	0.005
Kucharik	0.028	0.044	0.034	0.032	<i>0.025</i>	0.028
Fang	0.029	0.026	0.027	0.025	0.079	0.018
Gompertz	0.009	<i>0.016</i>	<i>0.010</i>	<i>0.018</i>	0.041	0.012

direction perpendicular to the row, it generally increases with increasing zenith angle. In the direction of the azimuth angle, the CI of the non-row structure scene varies randomly, and the variation range is relatively small, while the CI of the row structure scenes gradually increases from the row direction until it reaches the peak value in the direction perpendicular to the row.

Finally, based on the directional characteristics of the CI in the zenith angle, we proposed two models to fit the CI and compared them with other models. The results show that our model based on the Gompertz curve demonstrates higher accuracy ($R^2 = 0.98$) and the strongest stability, which is suitable for most

canopies, while the modified Montes model is the simplest with fewer input parameters. The directional CI can be effectively simulated when multiangle CI observations are insufficient. The study was based on the RAMI-V canopies, and the result of the CI was constrained by the reality of the scenes. Meanwhile, the analysis did not consider the influence of wood components on the gap fraction and CI, which are part of the clumping effect that also needs attention.

Appendix

Type	RAMI-ID	LAI	G (zenith=0)	Gap fraction (zenith=0)	CI (zenith=0)	
Abstract	HET10	0.9805	0.5028	0.80	0.46	
	HET11	0.9805	0.5028	0.80	0.46	
	HET12	0.9805	0.5028	0.80	0.46	
	HET16	1.6734	0.5028	0.70	0.42	
	HET17	2.4048	0.5028	0.60	0.42	
	HET18	3.2517	0.5028	0.48	0.45	
	HET20	1.9606	0.5028	0.63	0.47	
	HET21	1.9606	0.5028	0.63	0.47	
	HET22	1.9606	0.5028	0.63	0.47	
	HET23	0.3961	0.5026	0.86	0.75	
	HET24	1.5833	0.5028	0.55	0.75	
	HET26	2.6535	0.5028	0.56	0.44	
	HET27	3.3849	0.5028	0.48	0.44	
	HET28	4.2318	0.5026	0.38	0.45	
	HET33	0.3961	0.5028	0.84	0.87	
	HET34	1.5833	0.5028	0.51	0.85	
	HOM23	1	0.84	0.42	1.04	
	HOM24	1	0.84	0.42	1.04	
	HOM25	1	0.84	0.42	1.04	
	HOM26	5	0.77	0.01	1.45	
	HOM27	2	0.70	0.12	1.01	
	HOM28	1	0.64	0.27	1.02	
	HOM29	3	0.77	0.32	0.49	
	HOM30	2	0.53	0.34	1.00	
	HOM33	1	0.43	0.63	1.08	
	HOM34	1	0.43	0.63	1.08	
	HOM35	1	0.43	0.63	1.08	
	HOM36	5	0.50	0.05	0.98	
	HOM37	2	0.57	0.18	1.01	
	HOM38	1	0.64	0.27	1.02	
	Actual	HET07	2.2839	0.48	0.58	0.50
		HET08	0.6678	0.48	0.85	0.26
		HET09	3.4552	0.58	0.50	0.35
		HET14	2.6913	0.50	0.59	0.39
		HET15	0.0336	0.48	0.72	0.20
		HET16SRF	3.2086	0.72	0.59	0.23
		HET51	7.3396	0.77	0.10	0.41

Acknowledgments

We thank J. Qi of Beijing Forestry University for helping our team understand and use LESS.

Funding: The work is funded by the National Natural Science Foundation of China (grant nos. 42071304 and 42090013) and the National Key Research and Development Program of China (grant nos. 2020YFA0608701 and 2022YFB3903304).

Author contributions: J.X. and D.X. conceived the ideas, designed the methodology, and wrote the manuscript. J.X. and K.Z. provided codes and technology. D.X., G.Y., and X.M. provided suggestions regarding the data analysis.

Competing interests: The authors declare that they have no competing interests.

Data Availability

The directional CI dataset of RAMI-V scenes calculated based on this study is available on the website <http://lessrt.org>.

References

- Fang H. Canopy clumping index (CI): A review of methods, characteristics, and applications. *Agric. For. Meteorol.* 2021;303:Article 108374.
- Naudts K, Ryder J, McGrath MJ, Otto J, Chen Y, Valade A, Bellasen V, Berhongaray G, Bönisch G, Campioli M, et al. A vertically discretised canopy description for ORCHIDEE (SVN r2290) and the modifications to the energy, water and carbon fluxes. *Geosci. Model Dev.* 2015;8:2035–2065.
- Carrer D, Roujean J, Lafont S, Calvet JC, Boone A, Decharme B, Delire C, Gastellu-Etchegorry JP. A canopy radiative transfer scheme with explicit FAPAR for the interactive vegetation model ISBA-A-gs: Impact on carbon fluxes. *J. Geophys. Res. Biogeo.* 2013;118(2):888–903.
- Nouvellon Y, Bégué A, Moran MS, Lo Seen D, Rambal S, Luquet D, Chehbouni G, Inoue Y. PAR extinction in shortgrass ecosystems: Effects of clumping, sky conditions and soil albedo. *Agric. For. Meteorol.* 2000;105(1–3):21–41.
- Kucharik CJ, Norman JM, Gower ST. Characterization of radiation regimes in nonrandom forest canopies: Theory, measurements, and a simplified modeling approach. *Tree Physiol.* 1999;19(11):695–706.
- Baldocchi DD, Harley PC. Scaling carbon dioxide and water vapour exchange from leaf to canopy in a deciduous forest. II. Model testing and application. *Plant Cell Environ.* 1995;18(10):1157–1173.
- Watson DJ. Comparative physiological studies on the growth of field crops: I. Variation in net assimilation rate and leaf area between species and varieties, and within and between years. *Ann. Bot.* 1947;11:41–76.
- Bréda NJJ. Ground-based measurements of leaf area index: A review of methods, instruments and current controversies. *J. Exp. Bot.* 2003;54(392):2403–2417.
- Wei S, Fang H. Estimation of canopy clumping index from MISR and MODIS sensors using the normalized difference hotspot and darkspot (NDHD) method: The influence of BRDF models and solar zenith angle. *Remote Sens. Environ.* 2016;187:476–491.
- Chen JM. Remote sensing of leaf area index and clumping index. In: *Comprehensive remote sensing* Oxford: Elsevier; 2018. p. 53–77.
- Nilson T. *Agricultural meteorology*. Amsterdam: Elsevier; 1971. 25–38.
- Chen JM, Black TA. Defining leaf area index for non-flat leaves. *Plant Cell Environ.* 1992;15(4):421–429.
- Stenberg P. Correcting LAI-2000 estimates for the clumping of needles in shoots of conifers. *Agric. For. Meteorol.* 1996;79(1–2):1–8.
- Chen JM, Cihlar J. Plant canopy gap-size analysis theory for improving optical measurements of leaf-area index. *Appl. Optics.* 1995;34:6211–6222.
- Woodgate W, Disney M, Armston JD, Jones SD, Suarez L, Hill MJ, Wilkes P, Soto-Berelov M, Haywood A, Mellor A. An improved theoretical model of canopy gap probability for leaf area index estimation in woody ecosystems. *For. Ecol. Manage.* 2015;358:303–320.
- Jiao Z, Dong Y, Schaaf CB, Chen JM, Román M, Wang Z, Zhang H, Ding A, Erb A, Hill MJ, et al. An algorithm for the retrieval of the clumping index (CI) from the MODIS BRDF product using an adjusted version of the kernel-driven BRDF model. *Remote Sens. Environ.* 2018;209:594–611.
- Chen JM, Menges CH, Leblanc SG. Global mapping of foliage clumping index using multi-angular satellite data. *Remote Sens. Environ.* 2005;97:447–457.
- Leblanc SG, Chen JM, White HP, Latifovic R, Lacaze R, Roujean J-L. Canada-wide foliage clumping index mapping from multiangular POLDER measurements. *Can J Remote Sens.* 2005;31(5):364–376.
- Wei S, Fang H, Schaaf CB, He L, Chen JM. Global 500 m clumping index product derived from MODIS BRDF data (2001–2017). *Remote Sens. Environ.* 2019;232:Article 111296.
- Pisek J, Ryu Y, Sprintsin M, He L, Oliphant AJ, Korhonen L, Kuusk J, Kuusk A, Bergstrom R, Verrelst J, et al. Retrieving vegetation clumping index from Multi-angle Imaging SpectroRadiometer (MISR) data at 275m resolution. *Remote Sens. Environ.* 2013;138:126–133.
- He L, Chen JM, Pisek J, Schaaf CB, Strahler AH. Global clumping index map derived from the MODIS BRDF product. *Remote Sens. Environ.* 2012;119:118–130.
- Hill MJ, Román MO, Schaaf CB, Hutley L, Brannstrom C, Etter A, Hanan NP. Characterizing vegetation cover in global savannas with an annual foliage clumping index derived from the MODIS BRDF product. *Remote Sens. Environ.* 2011;115(8):2008–2024.
- Fang H, Liu W, Li W, Wei S. Estimation of the directional and whole apparent clumping index (ACI) from indirect optical measurements. *ISPRS J Photogramm Remote Sens.* 2018;144:1–13.
- Duthoit S, Demarez V, Gastellu-Etchegorry J, Martin E, Roujean J-L. Assessing the effects of the clumping phenomenon on BRDF of a maize crop based on 3D numerical scenes using DART model. *Agric. For. Meteorol.* 2008;148(8–9):1341–1352.
- Monsi M, Saeki T. On the factor light in plant communities and its importance for matter production. *Ann. Bot.* 2004;95(3):549–567.
- Braghiere RK, Quaié T, Black E, Ryu Y, Chen Q, de Kauwe MG, Baldocchi D. Influence of sun zenith angle on canopy clumping and the resulting impacts on photosynthesis. *Agric. For. Meteorol.* 2020;291:Article 108065.
- Fang H, Ye Y, Liu W, Wei S, Ma L. Continuous estimation of canopy leaf area index (LAI) and clumping index over broadleaf crop fields: An investigation of the PASTIS-57 instrument and smartphone applications. *Agric. For. Meteorol.* 2018;253–254:48–61.

28. Leblanc SG, Chen JM, Fernandes R, Deering DW, Conley A. Methodology comparison for canopy structure parameters extraction from digital hemispherical photography in boreal forests. *Agric. For. Meteorol.* 2005;129(3-4):187-207.
29. Leblanc SG. Correction to the plant canopy gap-size analysis theory used by the tracing radiation and architecture of canopies instrument. *Appl. Optics.* 2002;41:7667-7670.
30. Jiang H, Hu R, Yan G, Cheng S, Li F, Qi J, Li L, Xie D, Mu X. Influencing factors in estimation of leaf angle distribution of an individual tree from terrestrial laser scanning data. *Remote Sens. (Basel).* 2021;13(6):1159.
31. Garrigues S, Shabanov NV, Swanson K, Morisette JT, Baret F, Myneni RB. Intercomparison and sensitivity analysis of leaf area index retrievals from LAI-2000, AccuPAR, and digital hemispherical photography over croplands. *Agric. For. Meteorol.* 2008;148(8-9):1193-1209.
32. Yan G, Hu R, Luo L, Mu X, Xie D, Zhang W. Review of indirect methods for leaf area index measurement. *J Remote Sens.* 2016;20(5):958-978.
33. Chen JM, Black TA. Measuring leaf area index of plant canopies with branch architecture. *Agric. For. Meteorol.* 1991;57(1-3):1-12.
34. Miller JB. A formula for average foliage density. *Aust J Bot.* 1967;15(1):141-144.
35. Kuusk A. A Markov chain model of canopy reflectance. *Agric. For. Meteorol.* 1995;76:221-236.
36. Norman JM, Welles JM. Radiative-transfer in an array of canopies. *Agron. J.* 1983;75(1):481-488.
37. Warren Wilson J. Stand structure and light penetration. I. Analysis by point quadrats. *J. Appl. Ecol.* 1965;2:383-390.
38. Fang H, Li W, Wei S, Jiang C. Seasonal variation of leaf area index (LAI) over paddy rice fields in NE China: Intercomparison of destructive sampling, LAI-2200, digital hemispherical photography (DHP), and AccuPAR methods. *Agric. For. Meteorol.* 2014;198-199:126-141.
39. Montes F, Pita P, Rubio A, Cañellas I. Leaf area index estimation in mountain even-aged *Pinus silvestris* L. stands from hemispherical photographs. *Agric. For. Meteorol.* 2007;145(3-4):215-228.
40. Cohen S, Fuchs M. The distribution of leaf area, radiation, photosynthesis and transpiration in a Shamouti orange hedgerow orchard. Part I. Leaf area and radiation. *Agric. For. Meteorol.* 1987;40:123-144.
41. chneider FD, Leiterer R, Morsdorf F, Gastellu-Etchegorry JP, Lauret N, Pfeifer N, Schaepman ME. Simulating imaging spectrometer data: 3D forest modeling based on LiDAR and in situ data. *Remote Sens. Environ.* 2014;152:235-250.
42. Widlowski JL, Pinty B, Lopatka M, Atzberger C, Buzica D, Chelle M, Disney M, Gastellu-Etchegorry JP, Gerboles M, Gobron N, et al. The fourth radiation transfer model intercomparison (RAMI-IV): Proficiency testing of canopy reflectance models with ISO-13528. *J Geophys Res Atmos.* 2013;118:6869-6890.
43. Kuusk A, Pisek J, Lang M, Märdla S. Estimation of gap fraction and foliage clumping in forest canopies. *Remote Sens. (Basel).* 2018;10(7):1153.
44. Gastellu-Etchegorry JP, Demarez V, Pinel V, Zagolski F. Modeling radiative transfer in heterogeneous 3-D vegetation canopies. *Remote Sens. Environ.* 1996;58(2):131-156.
45. Qi J, Xie D, Yin T, Yan G, Gastellu-Etchegorry JP, Li L, Zhang W, Mu X, Norford LK. LESS: Large-Scale remote sensing data and image simulation framework over heterogeneous 3D scenes. *Remote Sens. Environ.* 2019;221:695-706.
46. Pinty B, Widlowski J-L, Taberner M, Gobron N, Verstraete MM, Disney M, Gascon F, Gastellu J-P, Jiang L, Kuusk A, et al. Radiation transfer model intercomparison (RAMI) exercise: Results from the second phase. *J Geophys Res Atmos.* 2004;109(D6):D6210.
47. Pinty B, Gobron N, Widlowski J, Gerstl SAW, Verstraete MM, Antunes M, Bacour C, Gascon F, Gastellu JP, Goel N, et al. Radiation transfer model intercomparison (RAMI) exercise. *J Geophys Res Atmos.* 2001;106:11937-11956.
48. Zhou K, Xie D, Qi J. Explicitly reconstructing RAMI-V scenes for accurate 3-dimensional radiative transfer simulation using the LESS model. *J Remote Sens.* 2023;3:0083.
49. Ma L, Li C, Tang B, Tang L, Bi Y, Zhou B, Li ZL. Impact of spatial LAI heterogeneity on estimate of directional gap fraction from SPOT-satellite data. *Sensors.* 2008;8:3767-3779.
50. Li X, Strahler AH. Geometric-optical bidirectional reflectance modeling of the discrete crown vegetation canopy: Effect of crown shape and mutual shadowing. *IEEE Trans. Geosci. Remote Sens.* 1992;30:276-292.
51. Ross J. *The radiation regime and architecture of plant stands.* The Hague, The Netherlands: Dr. W. Junk Publishers; 1981.
52. Tjørve KMC, Tjørve E. The use of Gompertz models in growth analyses, and new Gompertz-model approach: An addition to the Unified-Richards family. *PLOS ONE.* 2017;12(6):Article e0178691.
53. Song W, Mu X, Ruan G, Gao Z, Li L, Yan G. Estimating fractional vegetation cover and the vegetation index of bare soil and highly dense vegetation with a physically based method. *Int J Appl Earth Obs Geoinf.* 2017;58:168-176.
54. Pinty P, Lavergne T, Dickinson RE, Widlowski JL, Gobron N, Verstraete MM. Simplifying the interaction of land surfaces with radiation for relating remote sensing products to climate models. *J Geophys Res.* 2006;111:(D2).